Journal of Materials Chemistry B

PAPER

View Article Online
View Journal

Cite this: DOI: 10.1039/c4tb01788a

Fe_3O_4@$mSiO_2$ core–shell nanocomposite capped with disulfide gatekeepers for enzyme-sensitive controlled release of anti-cancer drugs†

Chunyu Yang,[a] Wei Guo,[a] Liru Cui,[b] Na An,[b] Ting Zhang,[b] Gang Guo,*[b] Huiming Lin*[a] and Fengyu Qu*[a]

Received 29th October 2014
Accepted 20th November 2014

DOI: 10.1039/c4tb01788a

www.rsc.org/MaterialsB

Multifunctional nanocarriers based on the magnetic Fe_3O_4 nanoparticle core and bis-(3-carboxy-4-hydroxy phenyl) disulfide ($R-S-S-R_1$) modified mesoporous silica shell (Fe_3O_4@$mSiO_2$@$R-S-S-R_1$) were synthesized for cancer treatment through passive targeting and enzyme-sensitive drug release. Anti-cancer drug doxorubicin (DOX) was used as the model cargo to reveal the release behavior of the system. The drug loading system (DOX–Fe_3O_4@$mSiO_2$@$R-S-S-R_1$) retains the drug until it reaches the tumor tissue where glutathione reductase (GSH) can degrade the disulfide bonds and release the drug. Furthermore, the grafting amount of $R-S-S-R_1$ can be used to adjust the release performance. All the release behaviors fit the Higuchi model very well and the release kinetics are predominated by disulfide bond degradation and mesoporous structure. With good bioactivity and targeted release performance, the system could play an important role in the development of intracellular delivery nanodevices for cancer therapy.

Introduction

The development of diverse kinds of nanoscale drug delivery systems such as polymers,[1] micelles,[2] liposomes,[3] dendrimers[4] and inorganic materials[5] for cancer treatment has received considerable attention and has become a major field in medical research in recent years. Among these, the increasing interest in mesoporous silica nanoparticles (MSNs) has been greatly enhanced because of their flexible and robust properties, including easy modification, excellent chemical stability, and outstanding biocompatibility.[6–10] Moreover, the uniform and tunable morphology/pore size, high pore volume and large surface area for MSNs ensure high loading of various drug molecules as well as smart transporting.[11–14] However, pure MSN materials always face some practical applicability limitations due to the premature or burst drug release within several hours after incubation *in vitro*.[15] Therefore, the intriguing concept of stimulus-responsive gatekeeping was introduced to regulate the cargo release and to optimize the application of MSNs in nanomedicine. Presently, nanoparticles, organic molecules and supramolecular nanovalves have been employed as "gatekeepers" for MSNs to show their well-controlled release performance. The controlled-release process can be regulated either by external stimuli such as thermal, light, electrostatic, magnetic actuation, and photoirradiation, or by internal stimuli such as pH and enzymes.[16–20] For instance, Yang and co-workers constructed a novel cancer theranostic hybrid platform, based on mesoporous silica-coated gold nanorods gated by sulfonatocalix[4]arene switches, for biofriendly near-infrared (NIR) light-triggered cargo release in a remote and stepwise fashion.[21] Zhu *et al.* successfully demonstrated a pH-triggered controlled drug release system by the dissolution of ZnO nanolids in acidic conditions, showing a valuable pH-responsive strategy for the delivery of anticancer agents.[22]

The disulfide bond is systemically nontoxic and stable in blood circulation, and it can only be degraded by reduced glutathione or other thiol compounds with certain concentrations.[23,24] Furthermore, the concentration of GSH is often elevated to 2–10 mM (ref. 25 and 26) in tumor tissues,[27,28] about twice that compared to normal tissues; thus, the disulfide bond is more attractive in its use in the targeted release on tumor tissues. For example, Yang *et al.* described the preparation of core–shell multi-sensitive composite nanoparticles with a poly(*N*-vinylcaprolactam-*s*-*s*-methacrylic acid) (P-(VCL-*s*-*s*-MAA)) shell to reveal the sensitive release behavior for cancer treatment.[15]

Strongly magnetic (Fe_3O_4 or γ-Fe_2O_3) nanoparticles with low toxicity have been most intensively studied as targeted and magnetic resonance imaging agents.[29–32] However, pure iron oxide is prone to aggregation due to anisotropic dipolar

[a]Department of Photoelectric Band Gap Materials Key Laboratory of Ministry of Education, Harbin Normal University, Harbin 150025, China. E-mail: qufengyu@hrbnu.edu.cn; linhuiming@hrbnu.edu.cn; Tel: +86 451-88060653

[b]College of Chemistry and Chemical Engineering, Harbin Normal University, Harbin 150025, China. E-mail: guogang19761126@sina.com

† Electronic supplementary information (ESI) available. See DOI: 10.1039/c4tb01788a

attraction and rapid biodegradation when they are exposed to biological systems directly.[33,34] The core–shell structure with iron oxide nanoparticles as the core and mesoporous silica as the shell not only can overcome the limitations of pure iron oxide nanoparticles but also can combine the advantages of the two to improve the performance in the field of targeted drug delivery.[35,36] Due to the collateral damage and adverse side effects of most cancer drugs, targeting drug delivery systems have attracted much attention for cancer therapy.[37] For example, Yang *et al.* designed novel fibrous-structured mesoporous silica microspheres (denoted as Fe_3O_4/FMSMs), which exhibited a sustained drug release profile, sufficient magnetic responsivity and redispersibility to the external magnetic field. In addition, Wang and coworkers synthesized a biocontrollable drug release system with PAH/PSS multilayers on Fe_3O_4/$mSiO_2$, which showed magnetic-targeting and pH-controllable release behavior.

With all of these considerations in mind, we synthesized a Fe_3O_4@$mSiO_2$ nanocarrier consisting of a magnetic Fe_3O_4 nanoparticle core and a mesoporous silica ($mSiO_2$) shell, which showed a passive targeting property (Fe_3O_4 target) associated with enzyme-sensitive controlled release. As shown in Scheme 1, in the first step, the core–shell Fe_3O_4@$mSiO_2$ nanomaterials were prepared as the drug carriers. At the same time, the synthesized bis-(3-carboxy-4-hydroxy phenyl) disulfide was modified with an amino silane coupling agent (3-aminopropyltriethoxysilane), denoted as (R–S–S–R_1). After the drug (DOX) loading, the enzyme-sensitive R–S–S–R_1 was employed to graft outside of the Fe_3O_4@$mSiO_2$ as the blocking agent to inhibit premature drug release. It is known that the high expression of glutathione reductase (GSH)[38] in tumor tissue promotes the degradation of –S–S–, thereby allowing the release of DOX.

Experiment and methods

Materials

Unless specified, all of the chemicals were analytical grade and were used without further purification. Cetyltrimethylammonium bromide (CTAB), tetraethyl orthosilicate (TEOS), 3-[4,5-dimethylthialzol-2-yl]-2,5-diphenyltetrazolium bromide (MTT), doxorubicin hydrochloride (DOX·HCl), 2′-(4-ethoxyphenyl)-5-(4-methyl-1-piperazinyl)-2,5′-bi-1*H*-benzimidazole, trihydrochloride (Hoechst 33342), *N*,*N*′-dicyclohexylcarbodiimide (DCC), 4-dimethylaminopyridine (DMAP), (3-aminopropyl)triethoxysilane (APTES), sodium oleate, oleic acid, 1-octadecene, 5-aminosalicyclic acid, sodium nitrite, potassium xantogenate, dichloromethane, ethyl acetate, and petroleum ether were obtained from Aladdin, China. Ferric trichloride hexahydrate ($FeCl_3 \cdot 6H_2O$), ethanol, *n*-hexane and triethylamine were purchased from Tianjin Chemical Corp. of China.

Synthesis of iron–oleate complex

In a typical synthesis of the iron–oleate complex, 10.8 g of iron chloride ($FeCl_3 \cdot 6H_2O$, 40 mmol) and 36.5 g of sodium oleate (120 mmol, 95%) were dissolved in a mixture composed of 80 mL ethanol, 60 mL distilled water and 140 mL hexane. The resulting solution was heated to 70 °C and maintained at that temperature for 4 h. When the reaction was complete, the upper organic layer containing the iron–oleate complex was washed three times with 30 mL distilled water in a separatory funnel. After washing, hexane was evaporated off, resulting in the iron–oleate complex in a waxy solid form.

Synthesis of Fe_3O_4 nanoparticles

Fe_3O_4 nanoparticles were prepared using a literature procedure.[39] 36 g (40 mmol) of the iron–oleate and 5.7 g of oleic acid (20 mmol, 90%) were dissolved in 200 g of 1-octadecene (90%) at room temperature. The reaction mixture was heated to 320 °C with a constant heating rate of 3.3 °C min^{-1}, and then kept at that temperature for 30 min. When the reaction temperature reached 320 °C, a dramatic reaction occurred and the initial transparent solution became turbid and brownish black. The resulting solution, containing the nanocrystals, was then cooled to room temperature, and 500 mL of ethanol was added to the solution to precipitate the nanocrystals, which were collected by centrifugation and then dispersed in chloroform.

Synthesis of Fe_3O_4@$mSiO_2$ nanoparticles

In a typical procedure, 0.5 mL of the Fe_3O_4 nanocrystals in chloroform (10 mg mL^{-1}) were poured into 8 mL of 0.2 M aqueous CTAB solution and the resulting solution was stirred vigorously for 30 min. The formation of an oil-in-water microemulsion resulted in a turbid brown solution. Then, the mixture was heated up to 60 °C for 30 min to evaporate the chloroform, resulting in a transparent black Fe_3O_4/CTAB solution. Next, 20 mL of distilled water was added to the obtained black solution and the pH value of the mixture was adjusted to 8–9 by using 0.1 M NaOH. After that, 100 μL of 20% TEOS in ethanol was injected six times at 30 min intervals. The reaction mixture was reacted for 24 h under violent stirring. The obtained Fe_3O_4@$mSiO_2$ NPs were centrifuged and rinsed with ethanol repeatedly to remove the excess precursors and CTAB molecules, and they were then dispersed in ethanol (8 mL).

Synthesis of bis-(3-carboxy-4-hydroxy phenyl) disulfide (R–S–S–R)

The disulfide was prepared from 5-ASA through the preparation of the xantogenate derivative (see Fig. S1†).[40,41] In a three necked round bottomed flask, 5-aminosalicyclic acid (5.0 g, 0.03 mol, 1 eq.) was suspended in water (17 mL) and acidified with concentrated hydrochloric acid (13 mL). The mixture was then cooled to 0 °C. A solution of sodium nitrite (2.3 g, 0.03 mol, 1 eq.) in water (16 mL) was added dropwise to the acidic solution, keeping the temperature below 5 °C, and the mixture was stirred for 1.5 h. The reaction pH was then raised to 5 using sodium hydroxide (50%) under a temperature below 5 °C. Potassium xantogenate (15.70 g, 3 eq.) was dissolved in water (15 mL) under nitrogen at room temperature: the cooled diazonium solution was added dropwise to the solution. The solution turned red and nitrogen gas was released. The reaction mixture was stirred for an additional hour at room temperature.

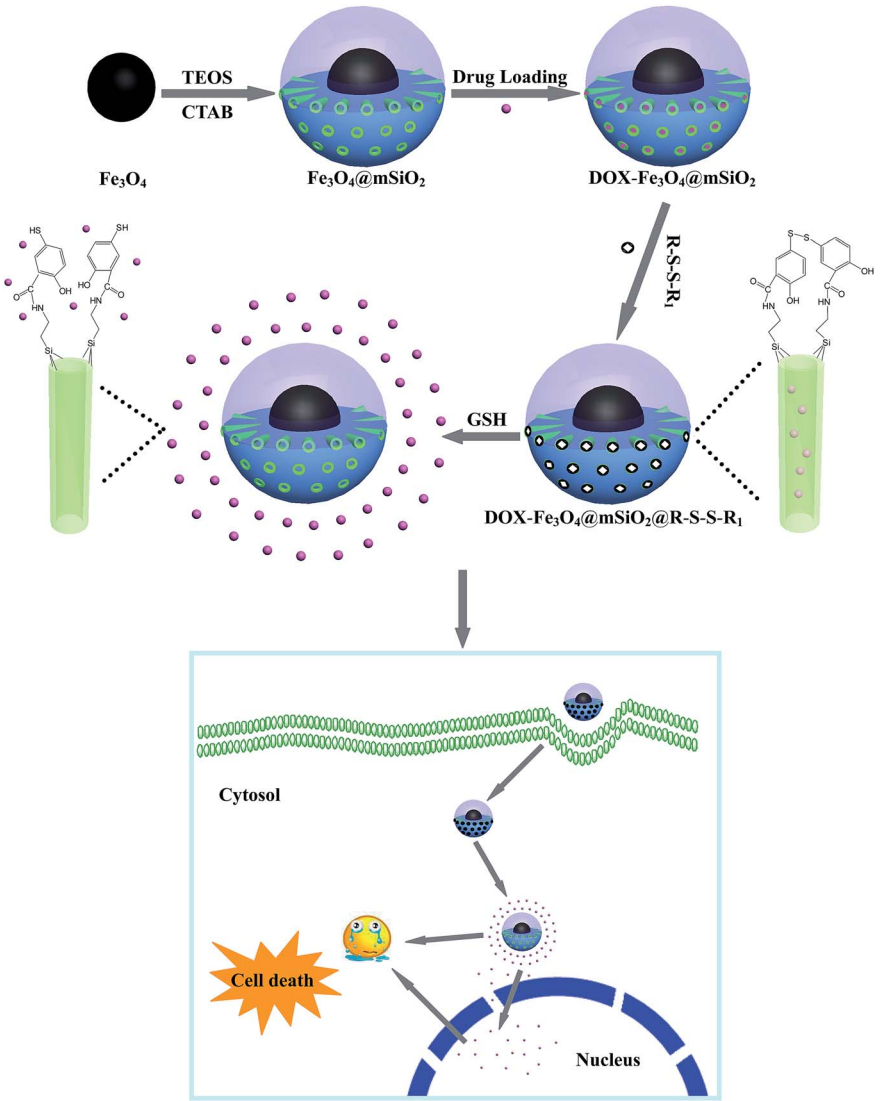

Scheme 1 Illustration of the preparation and controlled release process of DOX–Fe_3O_4@mSiO$_2$@R–S–S–R$_1$.

Dichloromethane was added and the mixture was acidified using 1 M hydrochloric acid. The organic phase was separated, extracted with brine, separated, dried and evaporated under reduced pressure. The residue was purified by flash column chromatography (PE : EA = 5 : 1) to give the xantogenate product (5.24 g, 62.16%). The product was dissolved in ethanol (22 mL) to give a red colored solution. Potassium hydroxide (3.41 g, 3 eq.) was added into this solution. The solution was stirred for 5 h, then acidified with 1 M HCl and extracted with ethyl acetate. The organic layer was separated, dried and evaporated. The crude product was purified by flash column chromatography on silica gel (PE : EA = 1 : 1) to obtain the disulfide (1.42 g, 12.85%). The NMR spectrum of as-synthesized R–S–S–R is shown in Fig. S2.†

Synthesis of R–S–S–R–APTES (R–S–S–R$_1$)

In a typical procedure, 3.718 g (0.011 mol) of R–S–S–R was dissolved in 50 mL of dimethyl sulfoxide at room temperature. When it was completely dissolved, 2.269 g (0.011 mol) of *N*,*N*′-dicyclohexylcarbodiimide (DCC) was added and then maintained at that temperature for 1 h. Then, 4.807 g (0.022 mol) of (3-aminopropyl)triethoxysilane (APTES) and 0.1222 g (0.001 mol) of 4-dimethylaminopyridine (DMAP) were added dropwise to the solution, and the reaction mixture was reacted for 28 h with stirring.

Drug loading and synthesis of DOX–Fe_3O_4@mSiO$_2$@R–S–S–R$_1$

Fe_3O_4@mSiO$_2$ (60 mg) and DOX (3 mg) were added to the ethanol solution (3 mL) and stirred at 25 °C for 12 h. Next, 150, 250 and 500 μL supernatant fluid of R–S–S–R$_1$ was added to the mixed solution. The obtained solid (named as DOX–Fe_3O_4@mSiO$_2$@R–S–S–R$_1$-1, DOX–Fe_3O_4@mSiO$_2$@R–S–S–R$_1$-2, DOX–Fe_3O_4@mSiO$_2$@R–S–S–R$_1$-3, respectively) was centrifuged, and washed several times with ethanol solution. The loading amount of DOX was determined by UV/vis spectroscopy at 480 nm. The loading efficiency (LE wt%) of DOX can be calculated

by using the formula (1). The experiment was repeated three times.

$$\text{LE wt\%} = \frac{m_{(\text{original DOX})} - m_{(\text{residual DOX})}}{m_{(\text{Fe}_3\text{O}_4@\text{mSiO}_2)} + m_{(\text{original DOX})} - m_{(\text{residual DOX})} + m_{(\text{R–S–S–R}_1)}} \times 100\% \quad (1)$$

Drug release

Gating protocol was investigated by studying the release profiles of DOX from the DOX–Fe_3O_4@mSiO_2@R–S–S–R_1 at pH 6.5 PBS buffer solution with 10 mM GSH or without GSH. Briefly, DOX–Fe_3O_4@mSiO_2@R–S–S–R_1 (30 mg) was dispersed in 5 mL of media solution and sealed in a dialysis bag (molecular weight cutoff 8000), which was submerged in 50 mL of media solution. At the interval time, the solution was taken out to determine the release amount by UV.

Cell culture

HeLa cells (cervical cancer cell line) and human umbilical vein endothelial cells (HUVEC) were grown in monolayers in Dulbecco's Modified Eagle's Medium (DMEM, Gibco) supplemented with 10% (v/v) fetal bovine serum (FBS, Tianhang bioreagent Co., Zhejiang) and penicillin/streptomycin (100 U mL^{-1} and 100 μg mL^{-1}, respectively, Gibco) in a humidified 5% CO_2 atmosphere at 37 °C.

Confocal laser scanning microscopy (CLSM)

To check cellular uptake, HeLa cells were cultured in a 12–well chamber slide with one piece of cover glass at the bottom of each chamber in the incubation medium (DMEM) for 24 h. The cell nucleus was labeled by Hoechst 33342. DOX–Fe_3O_4@mSiO_2@R–S–S–R_1-2 was added into the incubation medium at the concentration of 100 μg mL^{-1} for 6 h incubation in 5% CO_2 at 37 °C. After the medium was removed, the cells were washed twice with PBS (pH 7.4) and the cover glass was visualized under a laser scanning confocal microscope (FluoView FV1000, Olympus).

Cell viability

The viability of cells in the presence of nanoparticles was investigated using a 3-[4,5-dimethylthialzol-2-yl]-2,5-diphenyltetrazolium bromide (MTT, Sigma) assay. The assay was performed out in triplicate in the following manner. For the MTT assay, HeLa cells and HUVEC were seeded into 96-well plates at a density of 1×10^4 per well in 100 μL of media and grown overnight. The cells were then incubated with various concentrations of Fe_3O_4@mSiO_2, Fe_3O_4@mSiO_2@R–S–S–R_1-2 and DOX–Fe_3O_4@mSiO_2@R–S–S–R_1-2 for 24 h. Afterwards, cells were incubated in media containing 0.5 mg mL^{-1} of MTT for 4 h. The precipitated formazan violet crystals were dissolved in 100 μL of 10% SDS in 10 mmol HCl solution at 37 °C overnight. The absorbance was measured at 570 nm by a multi-detection microplate reader (Synergy™ HT, BioTek Instruments Inc, USA).

Characterization

Powder X-ray patterns (XRD) were recorded on a SIEMENSD 5005 X-ray diffractometer with Cu Kα radiation (40 kV, 30 mA). The nitrogen adsorption/desorption, surface areas, and median pore diameters were measured using a Micromeritics ASAP 2010M sorptometer. The surface area was calculated according to the conventional BET method and the adsorption branches of the isotherms were used for the calculation of the pore parameters using the BJH method. Fourier transform infrared (FTIR) spectra were recorded on a Perkin-Elmer 580B Infrared Spectrophotometer using the KBr pellet technique. A UV-vis spectrum was used to describe the amount of drug release (SHIMADZU UV2550 spectrophotometer). Transmission electron microscopy (TEM) images were recorded on TECNAI F20. Zeta potential and dynamic light scattering (DLS) were carried out with a ZetaPALS Zeta Potential Analyzer. The magnetic properties of samples were characterized with a Vibrating Sample Magnetometer (Lake Shore 7410).

Results and discussion

Morphology and structure

X-ray diffraction patterns of Fe_3O_4@mSiO_2, DOX–Fe_3O_4@mSiO_2@R–S–S–R_1-1, DOX–Fe_3O_4@mSiO_2@R–S–S–R_1–2, and DOX–Fe_3O_4@mSiO_2@R–S–S–R_1-3 powders are presented in Fig. 1. As can be seen in Fig. 1, all the samples reveal only one

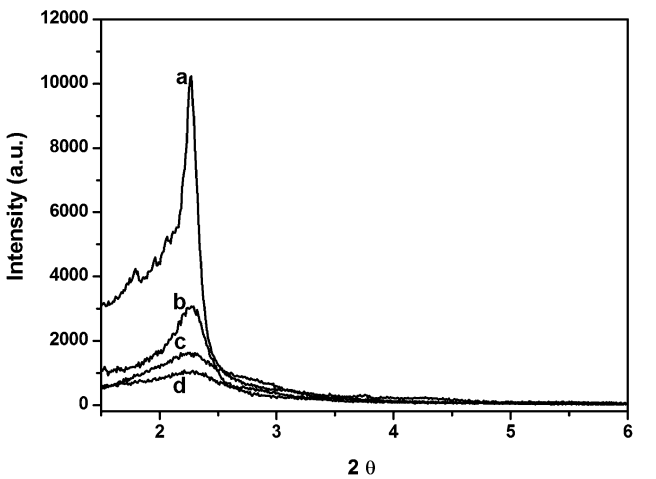

Fig. 1 Low-angle XRD patterns of (a) Fe_3O_4@mSiO_2, (b) DOX–Fe_3O_4@mSiO_2@R–S–S–R_1-1, (c) DOX–Fe_3O_4@mSiO_2@R–S–S–R_1-2, and (d) DOX–Fe_3O_4@mSiO_2@R–S–S–R_1-3.

diffraction peak at about $2\theta = 2.26°$, suggesting they all possess the mesoporous structure. Moreover, after drug loading and R–S–S–R_1 grafting, the diffraction intensities of DOX–Fe_3O_4@$mSiO_2$@R–S–S–R_1 undergo an obvious decrease. In addition, with increase in the R–S–S–R_1 that is grafted onto the Fe_3O_4@$mSiO_2$, there is a decrease in the diffraction intensity of DOX–Fe_3O_4@$mSiO_2$@R–S–S–R_1s, which is consistent with a previous report.[42]

The morphologies, particle sizes, and pores were investigated through TEM analysis. As displayed in Fig. 2A, Fe_3O_4 nanoparticles show the dispersed and uniform spherical morphology with an average diameter about 20 nm in size. Fe_3O_4@$mSiO_2$ reveals the obvious Fe_3O_4 core encapsulated by a 20 nm silica shell with a worm-like porous structure (Fig. 2B), which agrees with the corresponding XRD analysis (Fig. 1). As illustrated in Fig. 2C, the graft of the organic "gate" results in a rough surface and less dispersion of these nanoparticles.

The pore structure and related textural properties of Fe_3O_4@$mSiO_2$ and DOX–Fe_3O_4@$mSiO_2$@R–S–S–R_1s were investigated through nitrogen adsorption–desorption measurements. The corresponding adsorption isotherms and the pore size distribution curves are depicted in Fig. 3. From Fig. 3A, Fe_3O_4@$mSiO_2$ displays the typical IV adsorption isotherm and a steep capillary condensation step at a relative pressure of P/P_0 = 0.2–0.4. The typical H4 hysteresis loop is observed, testifying the mesoporous structure of Fe_3O_4@$mSiO_2$. As can be seen in Fig. 3A, there is a much smaller uptake of DOX–Fe_3O_4@$mSiO_2$@R–S–S–R_1 in comparison to its counterpart (Fe_3O_4@$mSiO_2$). This also makes the surface area and pore volume decrease from 326 $m^2\ g^{-1}$ and 0.285 $cm^3\ g^{-1}$ of Fe_3O_4@$mSiO_2$ to 115 $m^2\ g^{-1}$ and 0.118 $cm^3\ g^{-1}$ of DOX–Fe_3O_4@$mSiO_2$@R–S–S–R_1-1, 63.1 $m^2\ g^{-1}$ and 0.0839 $cm^3\ g^{-1}$ of DOX–Fe_3O_4@$mSiO_2$@R–S–S–R_1-2, 43.4 $m^2\ g^{-1}$ and 0.0605 $cm^3\ g^{-1}$ of DOX–Fe_3O_4@$mSiO_2$@R–S–S–R_1-3, respectively (Table 1).

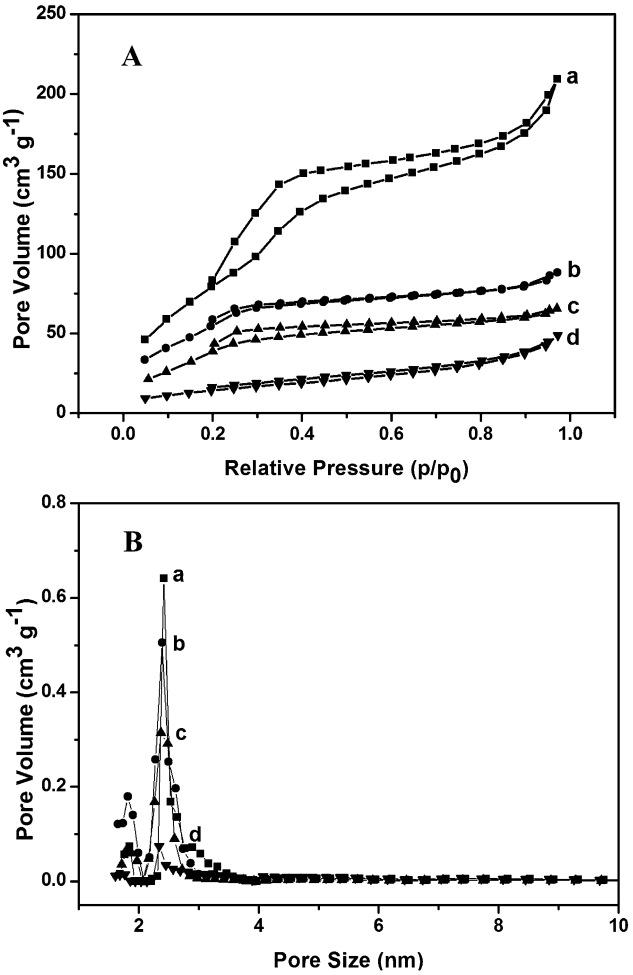

Fig. 3 (A) Nitrogen adsorption–desorption isotherms and (B) pore size distribution for (a) Fe_3O_4@$mSiO_2$, (b) DOX–Fe_3O_4@$mSiO_2$@R–S–S–R_1-1, (c) DOX–Fe_3O_4@$mSiO_2$@R–S–S–R_1-2, and (d) DOX–Fe_3O_4@$mSiO_2$@R–S–S–R_1-3.

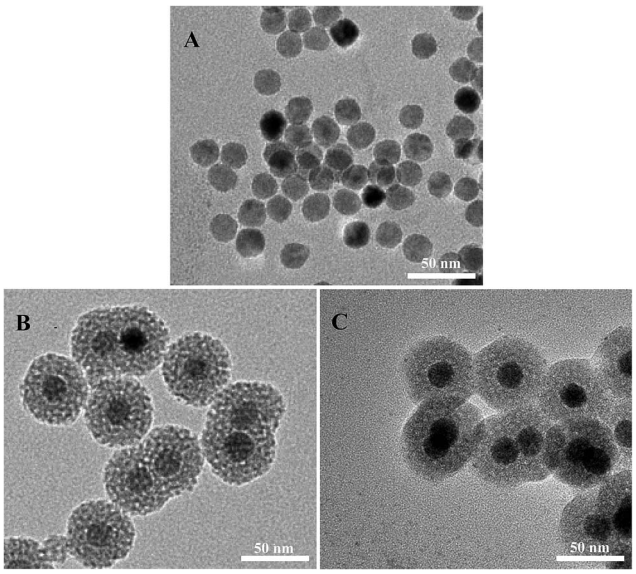

Fig. 2 TEM images of (A) Fe_3O_4, B) Fe_3O_4@$mSiO_2$, and C) Fe_3O_4@$mSiO_2$@R–S–S–R_1-2.

Furthermore, as displayed in Table 1, it is worth mentioning that with the highest packages of R–S–S–R_1, DOX–Fe_3O_4@$mSiO_2$@R–S–S–R_1-3 possesses the lowest surface area and pore volume.

The FTIR absorption spectrum measurement was carried out to investigate the presence of R–S–S–R_1 grafting after the modification. The corresponding FT-IR spectra of R–S–S–R, R–S–S–R–APTES, Fe_3O_4@$mSiO_2$ and Fe_3O_4@$mSiO_2$@R–S–S–R_1 are illustrated in Fig. 4. As depicted in Fig. 4A, the absorption bands at 1689 and 1662 cm^{-1} are assigned to the C=O stretching vibration of dicarboxylic acids, and the O–H deformation vibration and C–O stretching vibration bands at 1440 and 1290 cm^{-1} also can be clearly observed. Furthermore, the absorption bands at 1200 and 1599 cm^{-1} are assigned to the C–O stretching vibration and C=C stretching vibration of phenol, respectively. Moreover, the absorption band of S–S at 535 cm^{-1} appears in R–S–S–R, confirming that R–S–S–R has been successfully synthesized. After the link of APTES, two new peaks at 1078 (Si–O stretching vibration) and 1579 cm^{-1} (N–H formation vibration) appear, confirming that R–S–S–R–APTES

Table 1 Pore parameters of the samples

Samples	BET ($m^2\ g^{-1}$)	V_p ($cm^3\ g^{-1}$)	Pore size (nm)
Fe_3O_4@$mSiO_2$	326	0.285	2.42
DOX–Fe_3O_4@$mSiO_2$@R–S–S–R_1-1	115	0.118	2.39
DOX–Fe_3O_4@$mSiO_2$@R–S–S–R_1-2	63.1	0.0839	2.37
DOX–Fe_3O_4@$mSiO_2$@R–S–S–R_1-3	43.4	0.0605	2.33

has been successfully synthesized. As shown in Fig. 4B, comparing Fe_3O_4@$mSiO_2$@R–S–S–R_1 with Fe_3O_4@$mSiO_2$, the obvious absorption bands at 1661 cm^{-1}, which are assigned to the C═O stretching vibration of acid amide, can verify the successful grafting of R–S–S–R_1 on Fe_3O_4@$mSiO_2$.

In addition, the hydrodynamic diameters of Fe_3O_4@$mSiO_2$ and Fe_3O_4@$mSiO_2$@R–S–S–R_1-2 were measured using a Zeta Potential Analyzer. As displayed in Table 2, the hydrodynamic diameter of Fe_3O_4@$mSiO_2$ centers at 82.0 nm which is larger than that observed from TEM because of the hydrate layer in aqueous environment; moreover, it increases to 107.4 nm after the functional graft with the R–S–S–R_1 shell. Furthermore, the corresponding zeta-potential was further used to monitor the surface change between Fe_3O_4@$mSiO_2$ and Fe_3O_4@$mSiO_2$@R–S–S–R_1. From Fig. 5, Fe_3O_4@$mSiO_2$ shows a zeta potential of -15.01 ± 1.17 mV derived from the negative charge of surface Si–OH, which increases to 5.22 ± 1.91, 8.94 ± 0.91, and 10.45 ± 1.26 mV for Fe_3O_4@$mSiO_2$@R–S–S–R_1-1, Fe_3O_4@$mSiO_2$@R–S–S–R_1-2, and Fe_3O_4@$mSiO_2$@R–S–S–R_1-3, respectively, due to the decrease of surface Si–OH substituted by R–S–S–R_1. Based on the above investigation, it is clear that R–S–S–R_1 has been successfully grafted on the surface of Fe_3O_4@$mSiO_2$.

Fig. 6 presents the magnetization characterization of Fe_3O_4@$mSiO_2$@R–S–S–R_1-1, Fe_3O_4@$mSiO_2$@R–S–S–R_1-2, and Fe_3O_4@$mSiO_2$@R–S–S–R_1-3 at room temperature. The hysteresis loops (Fig. 6) indicate the super paramagnetism of all the materials. Furthermore, the saturation magnetizations (M_s) of Fe_3O_4@$mSiO_2$@R–S–S–R_1-1, Fe_3O_4@$mSiO_2$@R–S–S–R_1-2, and Fe_3O_4@$mSiO_2$@R–S–S–R_1-3 are about 20.9, 15.1, and 9.08 emu g^{-1}, respectively, and are ascribed to the non-magnetic $mSiO_2$ and R–S–S–R_1.

Drug loading and release profiles

To investigate the sensitive controlled release kinetics of the DOX–Fe_3O_4@$mSiO_2$@R–S–S–R_1 system, DOX was selected as the model drug to evaluate the loading and controlled release behaviors. The actual loading capacities of DOX are calculated to be 1.23 ± 0.4, 1.60 ± 0.3 and 2.16 ± 0.5 wt% for DOX–Fe_3O_4@$mSiO_2$@R–S–S–R_1-1, DOX–Fe_3O_4@$mSiO_2$@R–S–S–R_1-2 and DOX–Fe_3O_4@$mSiO_2$@R–S–S–R_1-3, respectively. The *in vitro* release profile of DOX from DOX–Fe_3O_4@$mSiO_2$@R–S–S–R_1 in PBS buffer (pH 6.5) in response to GSH (10 mM in PBS) is shown in Fig. 7A. As can be seen in Fig. 7A, without GSH, DOX–Fe_3O_4@$mSiO_2$@R–S–S–R_1 nanoparticles release little cargo, which is below 25% at 24 h. However, DOX can be released freely with the aid of GSH. As displayed in Fig. 7A, it takes 4 h to reach 45.16%, 36.50%, and 10.90% and about 24 h to reach the maximal amount 94.89%, 69.06%, and 42.76% for DOX–Fe_3O_4@$mSiO_2$@R–S–S–R_1-1, DOX–Fe_3O_4@$mSiO_2$@R–S–S–R_1-2 and DOX–Fe_3O_4@$mSiO_2$@R–S–S–R_1-3, respectively. The selective release is ascribed to the activity of the "gate". It is known that, –S–S– is a typical sensitive bond to some reducing agents, such as GSH, which can induce the bond breaking and "gate" open and drug release. Without GSH, R–S–S–R_1 blocks the pores of $mSiO_2$ encapsulating the cargo within the pores. Furthermore, the release performance of DOX–Fe_3O_4@$mSiO_2$ (without a "gate") in pH 6.5 with and without GSH was also studied. As illustrated in Fig. 7A, the release of DOX from DOX–Fe_3O_4@$mSiO_2$ is faster than that from DOX–Fe_3O_4@$mSiO_2$@R–S–S–R_1. Moreover, there is no obvious difference between the DOX release from DOX–Fe_3O_4@$mSiO_2$ with or without GSH. Based on the above investigation, the controlled drug release relies on the "–S–S– gate" sensitivity to GSH. Without GSH or the "–S–S–

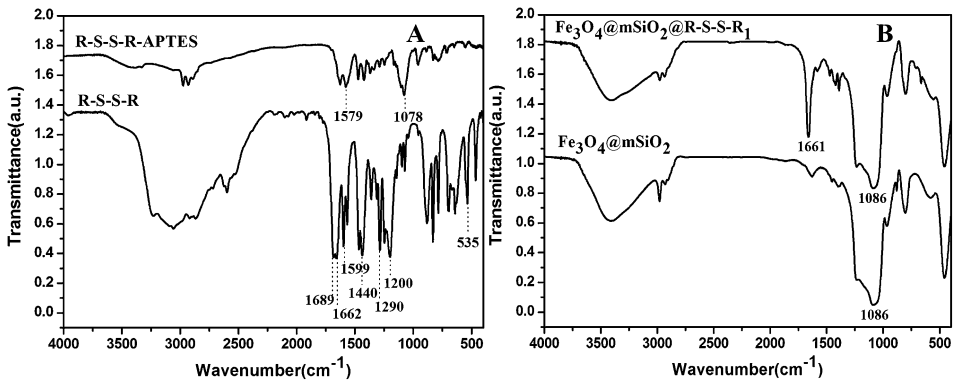

Fig. 4 FTIR spectra of (A) R–S–S–R and R–S–S–R–APTES and (B) Fe_3O_4@$mSiO_2$ and Fe_3O_4@$mSiO_2$@R–S–S–R_1.

Table 2 Hydrodynamic size of the samples

Samples	Hydrodynamic size distribution (nm)
Fe_3O_4@mSiO_2	82.0
Fe_3O_4@mSiO_2@R–S–S–R_1-2	107.4
Fe_3O_4@mSiO_2@R–S–S–R_1-2 after GSH treatment	110.3

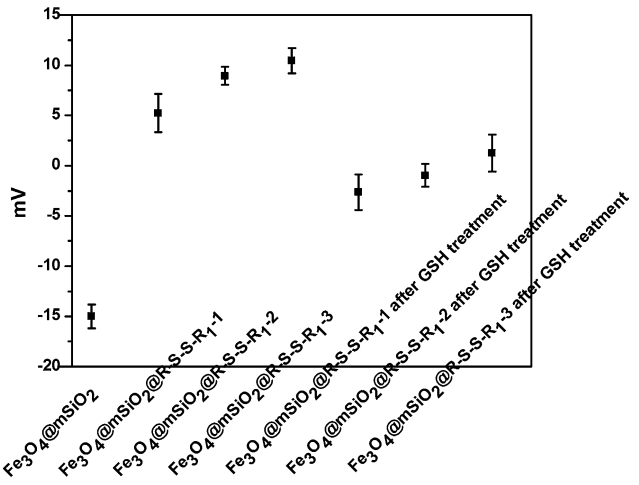

Fig. 5 Zeta potential test of Fe_3O_4@mSiO_2, Fe_3O_4@mSiO_2@R–S–S–R_1-1, Fe_3O_4@mSiO_2@R–S–S–R_1-2, Fe_3O_4@mSiO_2@R–S–S–R_1-3, Fe_3O_4@mSiO_2@R–S–S–R_1-1 after R–S–S–R_1 degraded in pH 6.5 with GSH, Fe_3O_4@mSiO_2@R–S–S–R_1-2 after R–S–S–R_1 degraded in pH 6.5 with GSH, Fe_3O_4@mSiO_2@R–S–S–R_1-3 after R–S–S–R_1 degraded in pH 6.5 with GSH.

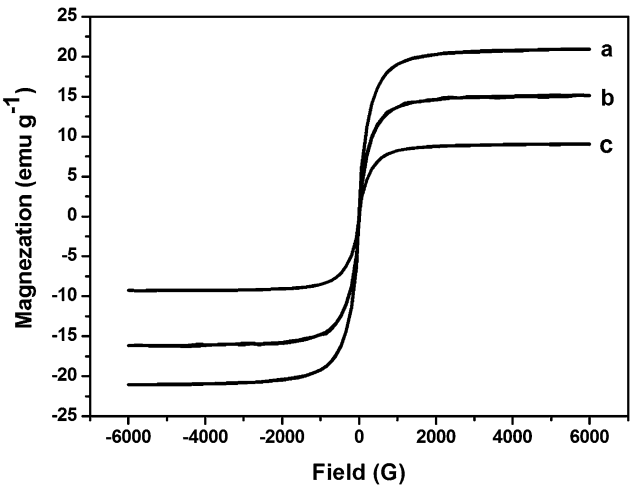

Fig. 6 Representative hysteresis loop measurements of the obtained (a) Fe_3O_4@mSiO_2@R–S–S–R_1-1, (b) Fe_3O_4@mSiO_2@R–S–S–R_1-2, and (c) Fe_3O_4@mSiO_2@R–S–S–R_1-3.

gate", controlled drug release performance can be obtained. The sensitive releases were further studied by the analysis of the hydrodynamic diameters and zeta-potentials before and after Fe_3O_4@mSiO_2@R–S–S–R_1s were treated by GSH. From Table 2, the hydrodynamic diameter increases from 107.4 to 110.3 nm, ascribed to the breaking of –S–S– outside Fe_3O_4@mSiO_2@R–S–S–R_1-2. Furthermore, the zeta potential also reduced from 5.22 ± 1.91, 8.94 ± 0.91, and 10.45 ± 1.26 mV to -2.64 ± 1.78, -0.97 ± 1.14, and 1.25 ± 1.84 mV, respectively, due to the breaking of –S–S– to form –SH (Fig. 5).

To further investigate the release behavior, the release data are analyzed by the Higuchi model.[43,44] As is well known, drug release kinetics from an insoluble, porous carrier matrix are frequently described by the Higuchi model, and the release rate can be described by the following equation:

$$Q = k \times t^{1/2} \quad (2)$$

where Q is the quantity of drug released from the materials, t denotes time, and k is the Higuchi dissolution constant. According to the model, for a purely diffusion-controlled process, the linear relationship is valid for the release of relatively small molecules distributed uniformly throughout the carrier.[44]

As illustrated in Fig. 7B, DOX–Fe_3O_4@mSiO_2@R–S–S–R_1-1 and DOX–Fe_3O_4@mSiO_2@R–S–S–R_1-2 exhibit a two-step release (0–8 h and 8–24 h) based upon the Higuchi model. Compared with the other two samples, DOX–Fe_3O_4@mSiO_2@R–S–S–R_1-3 just displays a one-step release within 24 h. In the first 8 h, DOX–Fe_3O_4@mSiO_2@R–S–S–R_1-1 possess the highest dissolution constant k (the slope of the fitting line), followed by DOX–Fe_3O_4@mSiO_2@R–S–S–R_1-2 and DOX–Fe_3O_4@mSiO_2@R–S–S–R_1-3. This is because when DOX–Fe_3O_4@mSiO_2@R–S–S–R_1s immerses in the release media with GSH, it induces –S–S– breaking and drug release. With the lowest amount of R–S–S–R_1, the "gatekeeper" was degraded most quickly, making the highest dissolution constant k as well as the fastest release rate of DOX–Fe_3O_4@mSiO_2@R–S–S–R_1-1. In the second release step (8–24 h), the release rates of DOX–Fe_3O_4@mSiO_2@R–S–S–R_1-1 and DOX–Fe_3O_4@mSiO_2@R–S–S–R_1-2 decrease, and tend to be similar to each other. It is believed that, in the first release step, most drug molecules release outside after the "gatekeeper" is broken. Thus, the first release step depends mainly upon the degradation of –S–S– and the second release step is determined just by the mesoporous structure of the host. However, with highest amount of R–S–S–R_1, the breaking of the "gatekeeper" is slow, which is associated with the mesoporous structure controlling the resistant release; therefore, DOX–Fe_3O_4@mSiO_2@R–S–S–R_1-3 displays a first-step release behavior for 24 h. To sum up, the amount of "gate" (R–S–S–R_1) can be used to regulate the release performance of the system.

In vitro cytotoxic effect and cellular uptake

To investigate the cellular uptake of the sample, DOX–Fe_3O_4@mSiO_2@R–S–S–R_1-2 was incubated with HeLa cells at the concentration of 100 μg mL^{-1} for 6 h. The cellular uptake and subsequent localization of the sample is shown in Fig. 8. As depicted in Fig. 8, nanoparticles are localized in the cytoplasm after 6 h incubation with HeLa cells, which proves the fast cellular uptake ability of the sample. This is ascribed to small particle size (65 nm), which is beneficial in entering the cell and

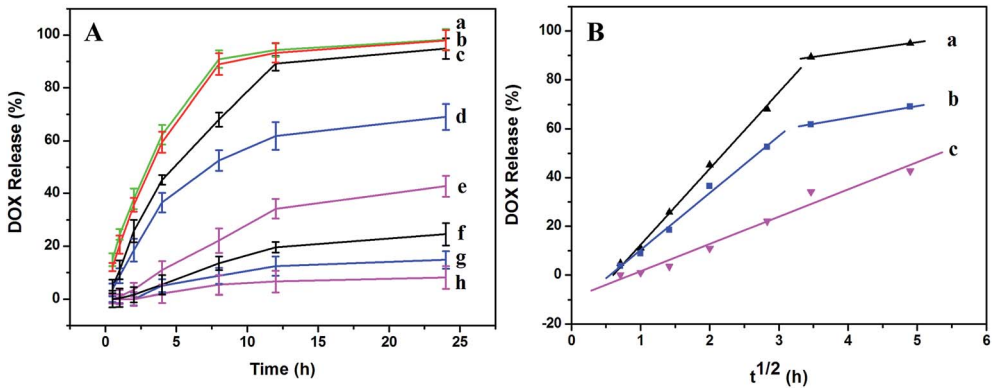

Fig. 7 Release profiles of DOX from (A) DOX–Fe_3O_4@$mSiO_2$ in pH 6.5 (a) with GSH, (b) without GSH, and DOX–Fe_3O_4@$mSiO_2$@R–S–S–R_1 in pH 6.5 with GSH (c) DOX–Fe_3O_4@$mSiO_2$@R–S–S–R_1-1, (d) DOX–Fe_3O_4@$mSiO_2$@R–S–S–R_1-2 (e) DOX–Fe_3O_4@$mSiO_2$@R–S–S–R_1-3, and DOX–Fe_3O_4@$mSiO_2$@R–S–S–R_1 in pH 6.5 without GSH, (f) DOX–Fe_3O_4@$mSiO_2$@R–S–S–R_1-1, (g) DOX–Fe_3O_4@$mSiO_2$@R–S–S–R_1-2, and (h) DOX–Fe_3O_4@$mSiO_2$@R–S–S–R_1-3; (B) Higuchi plot for the release of DOX from DOX–Fe_3O_4@$mSiO_2$@R–S–S–R_1 in pH 6.5 with GSH, (a) DOX–Fe_3O_4@$mSiO_2$@R–S–S–R_1-1, (b) DOX–Fe_3O_4@$mSiO_2$@R–S–S–R_1-2, and (c) DOX–Fe_3O_4@$mSiO_2$@R–S–S–R_1-3.

enhancing the drug efficacy.[45,46] In addition, DOX can also be found in cytoplasm after 6 h incubation and benefits from the fast cellular uptake ability of these nanocomposites and the low pH endosomal environment.[47] Importantly, the morphology of the HeLa cells was not influenced by the addition of DOX–Fe_3O_4@$mSiO_2$@R–S–S–R_1-2, also illustrating the good biocompatibility of the nanocomposites.

The investigation of the cytotoxicity of the synthesized drug carrier is significant for its potential biomedical applications. Only nontoxic carriers are suitable for drug delivery. Here, the cellular toxicity of Fe_3O_4@$mSiO_2$, Fe_3O_4@$mSiO_2$@R–S–S–R_1-2, and DOX–Fe_3O_4@$mSiO_2$@R–S–S–R_1-2 nanoparticles toward HeLa cells were determined by means of a standard MTT cell assay. It could be seen that both pure Fe_3O_4@$mSiO_2$ and Fe_3O_4@$mSiO_2$@R–S–S–R_1-2 show no significant cytotoxic effect on the HeLa cells in a range of concentrations (3.125–50 μg mL^{-1}). As can be seen in Fig. 9, the cell viability is 86.14% even after the concentration of Fe_3O_4@$mSiO_2$@R–S–S–R_1-2 reaches 50 μg mL^{-1}, while that of DOX–Fe_3O_4@$mSiO_2$@R–S–S–R_1-2 decreases to 58.79% death at 50 μg mL^{-1}. This can be explained by the fact that the nanoparticles can diffuse into cells rapidly, followed by the enzyme (GSH) inducing release of the anticancer drug DOX to make the higher cytotoxicity of DOX–Fe_3O_4@$mSiO_2$@R–S–S–R_1-2. In order to validate the specificity of the enzyme dependent

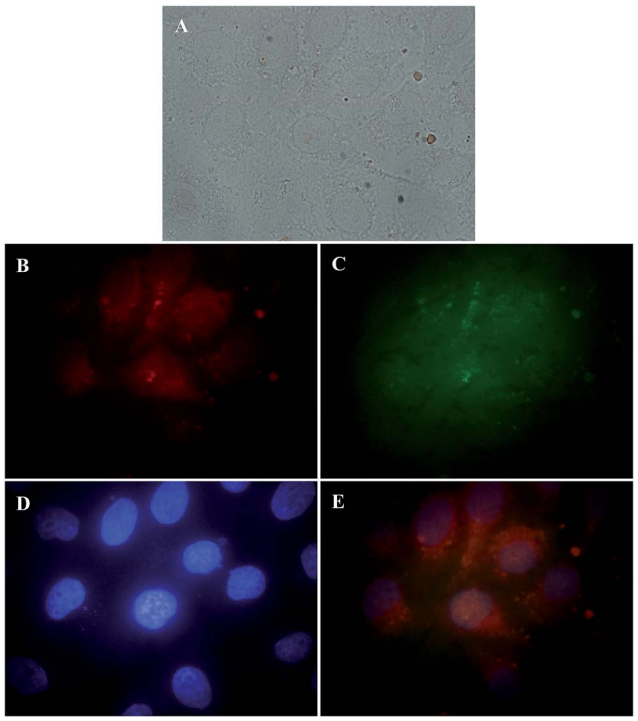

Fig. 8 CLSM images of HeLa cells after incubation with 100 μg mL^{-1} DOX–Fe_3O_4@$mSiO_2$@R–S–S–R_1-2 for 6 h. (A) HeLa cells (bright), (B) DOX fluorescence in cells (red), (C) FITC labeled DOX–Fe_3O_4@$mSiO_2$@R–S–S–R_1-2 (green), (D) Hoechst 33342 labeled cell nucleus (blue), and (E) merged.

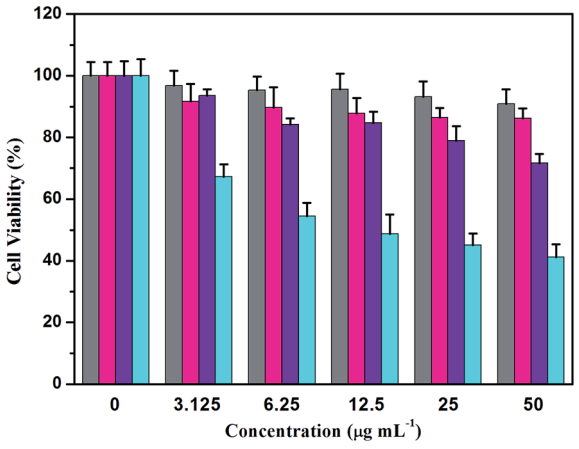

Fig. 9 Cell viability of HeLa cells incubated with different amounts of Fe_3O_4@$mSiO_2$ (gray), Fe_3O_4@$mSiO_2$@R–S–S–R_1-2 (pink), and DOX–Fe_3O_4@$mSiO_2$@R–S–S–R_1-2 (cyan), and human umbilical vein endothelial cells (HUVEC) incubated with different amounts of DOX–Fe_3O_4@$mSiO_2$@R–S–S–R_1-2 (violet) for 24 h.

drug release, DOX–Fe_3O_4@mSiO_2@R–S–S–R_1-2 incubated with a non-cancerous cell line (HUVEC) is presented as the control. As illustrated in Fig. 9, it shows a very low cytotoxic effect (about 28.40%) on the HUVEC even when the concentration of the cells reaches 50 μg mL^{-1} due to the lack of GSH to enhance DOX release.

Conclusion

In summary, we have demonstrated an enzyme-responsive controlled-release system using a smart switch (R–S–S–R_1) gated core–shell Fe_3O_4@mSiO_2 nanomaterial for targeted drug delivery. Owing to the degradation of the "gate," the cargo release is triggered by GSH, which is a specific enzyme that has been proved to be highly expressed at the tumor microenvironment. The *in vitro* efficacy of the nanocomposites were confirmed using HeLa cells and a MTT assay and CLSM were carried out, revealing that the nanocarrier can rapidly enter into the cells and has no obvious cytotoxic effect on HeLa cells at a concentration of 50 μg mL^{-1}. Furthermore, the drug molecules can be transported into cells just after 6 h incubation with HeLa. Considering the high specificity and good controlled-release performance, DOX–Fe_3O_4@mSiO_2@R–S–S–R_1 can be employed as a potential candidate for targeted cancer treatment.

Acknowledgements

Financial support for this study was provided by the National Natural Science Foundation of China (21471041, 21171045, 21101046, 21441002), the Natural Science Foundation of Heilongjiang Province of China ZD201214, and the Technology development pre-project of Harbin Normal University (12XYG-11).

References

1 F. S. Du, Y. Wang, R. Zhang and Z. C. Li, *Soft Matter*, 2010, **6**, 835–848.
2 J. Wu, Y. J. Zhu, F. Chen, X. Y. Zhao, J. Zhao and C. Qi, *Dalton Trans.*, 2013, **42**, 7032–7040.
3 X. Q. An, F. Zhan and Y. Y. Zhu, *Langmuir*, 2013, **29**, 1061–1068.
4 T. Levis and V. Ganesan, *Soft Matter*, 2012, **8**, 11817–11830.
5 A. Shimoda, S. I. Sawada, A. Kano, A. Maruyama, A. Moquin, F. M. Winnik and K. Akiyoshi, *Colloids Surf., B*, 2012, **99**, 38–44.
6 H. Kim, S. Kim, C. Park, H. Lee, H. J. Park and C. Kim, *Adv. Mater.*, 2010, **22**, 4280–4283.
7 Y. N. Zhao, B. G. Trewyn, I. I. Slowing and V. S.-Y. Lin, *J. Am. Chem. Soc.*, 2009, **131**, 8398–8400.
8 B. G. Trewyn, I. I. Slowing, S. Giri, H. T. Chen and V. S. Y. Lin, *Acc. Chem. Res.*, 2007, **40**, 846–853.
9 J. Lu, M. Liong, Z. X. Li, J. I. Zink and F. Tamanoi, *Small*, 2010, **6**, 1794–1805.
10 H. Yamada, C. Urata, Y. Aoyama, S. Osada, Y. Yamauchi and K. Kuroda, *Chem. Mater.*, 2012, **24**, 1462–1471.
11 L. Yuan, Q. Tang, D. Yang, J. Z. Zhang, F. Zhang and J. Hu, *J. Phys. Chem. C*, 2011, **115**, 9926–9932.
12 X. F. Guo, Y. S. Kim and G. J. Kim, *J. Phys. Chem. C*, 2009, **113**, 8313–8319.
13 M. Manzano and M. Vallet-Regi, *J. Mater. Chem.*, 2010, **20**, 5593–5604.
14 Y. J. Wang and F. Caruso, *Chem. Mater.*, 2005, **17**, 953–961.
15 B. S. Chang, D. Chen, Y. Wang, Y. Z. Chen, Y. F. Jiao, X. Y. Sha and W. L. Yang, *Chem. Mater.*, 2013, **25**, 574–585.
16 M. W. Ambrogio, C. R. Thomas, Y.-L. Zhao, J. I. Zink and J. F. Stoddart, *Acc. Chem. Res.*, 2011, **44**, 903–913.
17 S. Angelos, N. M. Khashab and Y.-W. Yang, *J. Am. Chem. Soc.*, 2009, **131**, 12912–12914.
18 B. S. Chang, X. Y. Sha, J. Guo, Y. F. Jiao, C. C. Wang and W. L. Yang, *J. Mater. Chem.*, 2011, **21**, 9239–9247.
19 E. Aznar, M. D. Marcos, R. Martinez-Manez, F. Sancenon, J. Soto, P. Amoros and C. Guillem, *J. Am. Chem. Soc.*, 2009, **131**, 6833–6843.
20 Y. Zhu, W. Meng, H. Gao and N. Hanagata, *J. Phys. Chem. C*, 2011, **115**, 13630–13636.
21 H. Li, L. L. Tan, P. Jia, Q. L. Li, Y. L. Sun, J. Zhang, Y. Q. Ning, J. H. Yu and Y. W. Yang, *Chem. Sci.*, 2014, **5**, 2804–2808.
22 F. Muhammad, M. Y. Guo, W. X. Qi, F. X. Sun, A. F. Wang, Y. J. Guo and G. S. Zhu, *J. Am. Chem. Soc.*, 2011, **133**, 8778–8781.
23 I. Ojima, *Acc. Chem. Res.*, 2008, **41**, 108–119.
24 I. Ojima, X. D. Geng, X. Y. Wu, C. X. Qu, C. P. Borella, H. S. Xie, S. D. Wilhelm, B. A. Leece, L. M. Bartle, V. S. Goldmacher and R. V. J. Chari, *J. Med. Chem.*, 2002, **45**, 5620–5623.
25 N. S. Kosower and E. M. Kosower, *Int. Rev. Cytol.*, 1978, **54**, 109–160.
26 S. J. Yu, C. L. He, J. X. Ding, Y. L. Cheng, W. T. Song, X. L. Zhuang and X. S. Chen, *Soft Matter*, 2013, **9**, 2637–2645.
27 J. A. Cook, H. I. Pass, S. N. Iype, N. Friedman, W. Degraff, A. Russo and J. B. Mitchell, *Cancer Res.*, 1991, **51**, 4287–4294.
28 S. L. Blair, P. Heerdt, S. Sacher, A. Abolhoda, S. Hochwald, H. Cheng and M. Burt, *Cancer Res.*, 1997, **57**, 152–155.
29 R. Weissleder, A. Bogdanov, E. A. Neuwelt and M. Papisov, *Adv. Drug Delivery Rev.*, 1995, **16**, 321–334.
30 J. Su, M. Cao, L. Ren and C. Hu, *J. Phys. Chem. C*, 2011, **115**, 14469–14477.
31 X. Li, X. Huang, D. Liu, X. Wang, S. Song, L. Zhou and H. Zhang, *J. Phys. Chem. C*, 2011, **115**, 21567–21573.
32 E. Taboada, E. Rodríguez, A. Roig, J. Oró, A. Roch and R. N. Muller, *Langmuir*, 2007, **23**, 4583–4588.
33 E. Ruiz-Hernández, A. López-Noriega, D. Arcos, I. Izquierdo-Barba, O. Terasaki and M. Vallet-Regí, *Chem. Mater.*, 2007, **19**, 3455–3463.
34 J. Zhou, W. Wu, D. Caruntu, M. H. Yu, A. Martin, J. F. Chen, C. J. O'Connor and W. L. Zhou, *J. Phys. Chem. C*, 2007, **111**, 17473–17477.
35 Y. Zhu, T. Ikoma, N. Hanagata and S. Kaskel, *Small*, 2010, **6**, 471–478.
36 M. Liong, J. Lu, M. Kovochich, T. Xia, S. G. Ruehm, A. E. Nel, F. Tamanoi and J. I. Zink, *ACS Nano*, 2008, **2**, 889–896.
37 P. P. Yang, S. L. Gai and J. Lin, *Chem. Soc. Rev.*, 2012, **41**, 3679–3698.

38 Z. B. Zheng and D. J. Creighton, *Bioconjugate Chem.*, 2005, **16**, 598–607.
39 J. Park, K. An, Y. H. Wang, J. G. Park, H. J. Noh, J. Y. Kim and T. Hyeon, *Nat. Mater.*, 2004, **3**, 891–895.
40 S. Saphier, A. Haft and S. Margel, *J. Med. Chem.*, 2012, **55**, 10781–10785.
41 D. A. Kennedy, N. Vembu, F. R. Fronczek and M. Devocelle, *J. Org. Chem.*, 2011, **76**, 9641–9647.
42 W. Guo, C. Y. Yang, L. R. Cui, H. M. Lin and F. Y. Qu, *Langmuir*, 2014, **30**, 243–249.
43 T. Higuchi, *J. Pharm. Sci.*, 1961, **50**, 874–875.
44 T. Higuchi, *J. Pharm. Sci.*, 1963, **52**, 1145–1149.
45 X. J. Song, H. Gong, S. N. Yin, L. Cheng, C. Wang, Z. W. Li, Y. G. Li, X. Y. Wang, G. Liu and Z. Liu, *Adv. Funct. Mater.*, 2014, **24**, 1194–1201.
46 L. M. Pan, Q. J. He, J. N. Liu, Y. Chen, M. Ma, L. L. Zhang and J. L. Shi, *J. Am. Chem. Soc.*, 2012, **134**, 5722–5725.
47 X. Zhang, P. P. Yang, Y. L. Dai, P. A. Ma, X. J. Li, Z. Y. Cheng, Z. Y. Hou, X. J. Kang, C. X. Li and J. Lin, *Adv. Funct. Mater.*, 2013, **23**, 4067–4078.

